# Faraday Discussions

## Accepted Manuscript


This manuscript will be presented and discussed at a forthcoming Faraday Discussion meeting. All delegates can contribute to the discussion which will be included in the final volume.

**Register now to attend!** Full details of all upcoming meetings: **http://rsc.li/fd-upcoming-meetings**


This is an *Accepted Manuscript*, which has been through the RSC Publishing peer review process and has been accepted for publication.

*Accepted Manuscripts* are published online shortly after acceptance, which is prior to technical editing, formatting and proof reading. This free service from RSC Publishing allows authors to make their results available to the community, in citable form, before publication of the edited article. This *Accepted Manuscript* will be replaced by the edited and formatted *Advance Article* as soon as this is available.

To cite this manuscript please use its permanent Digital Object Identifier (DOI®), which is identical for all formats of publication.

More information about *Accepted Manuscripts* can be found in the **Information for Authors**.

Please note that technical editing may introduce minor changes to the text and/or graphics contained in the manuscript submitted by the author(s) which may alter content, and that the standard **Terms & Conditions** and the **ethical guidelines** that apply to the journal are still applicable. In no event shall the RSC be held responsible for any errors or omissions in these *Accepted Manuscript* manuscripts or any consequences arising from the use of any information contained in them.

# Diffusion of Atomic Oxygen Relevant to Water Formation in Amorphous Interstellar Ices

**Myung Won Lee and Markus Meuwly***

***Received Xth XXXXXXXXXX 20XX, Accepted Xth XXXXXXXXX 20XX***
***First published on the web Xth XXXXXXXXXX 20XX***
**DOI: 10.1039/c000000x**

Molecular dynamics (MD) simulations together with accurate physics-based force fields are employed to determine the mobility of atomic oxygen in amorphous ice at low temperatures, characteristic for conditions in interstellar ices. From the simulations it is found that the mobility of atomic oxygen ranges from 60 to 480 Å$^2$/ns in amorphous ice at temperatures between 50 and 200 K. Hence, the simulations establish that atomic oxygen is mobile to a certain degree and chemical mechanisms for water formation involving oxygen mobility is a realistic scenario. This is also confirmed from the computed migration barriers for oxygen diffusion by multiple umbrella sampling simulations which yield barriers for diffusion in the range of 0.7 – 1.9 kcal/mol. The physics-based force field - based on a multipolar expansion of the electrostatic interactions - yields more pronounced energetics for oxygen migration pathways compared to the conventional point-charge models employed in typical simulations. Once formed, the computed solvation free energy suggests that atomic oxygen thermodynamically prefers to be localized inside amorphous ice and is available for chemical reaction which may be relevant to water formation in and on grains.

## 1 Introduction

Water is an essential component in astrophysical environments where it has been detected in various forms. Bulk water itself is present in the form of amorphous solid water (ASW) which is the main

Department of Chemistry, University of Basel, Klingelbergstrasse 80, 4056 Basel, Switzerland

component of interstellar ices.[1] The structure – and transitions between different forms – of ASW is typically inferred from spectroscopic measurements[1,2] although recently, an interference-based method has also been employed.[3] ASW is able to support a highly porous structure which is characterized by large scale internal cavities which can potentially retain large quantities of guest species in molecular or atomic form.[4] Under laboratory conditions the water ices seem to be amorphous in nature[5] whereas the morphology of ices in the interstellar medium are more debatable.[6]

It is believed that pristine water can be formed and grows on the icy dust grains in interstellar clouds from hydrogen and oxygen atoms, due to the inefficiency of the gas-phase formation of water.[7–10] At present, however, little is known about the mechanisms underlying water formation in and on dust grains, where the amorphous form of water seems to dominate. A Monte Carlo study showed that the prevalence of a particular water formation channel depends on the local environment.[7] In translucent and diffuse clouds (with temperatures $T \lesssim 50$ K)[11] the main route went through the atomic oxygen channel whereas the molecular oxygen ($O_2$) together with the ozone ($O_3$) route dominated in dense cold molecular clouds ($T \sim 10$ K).[7] The reactions leading to water formation through atomic and molecular oxygen and ozone have been studied extensively over the past few years.[12–15]

Independent of the particular reaction channel(s) assumed, atomic oxygen plays an essential role in water formation.[16] Several scenarios for the elementary reaction steps involved in water formation under astrophysical and interstellar conditions have been put forward in the past.[13,16–19] As reaction partners within an assumed reaction network are not necessarily generated or present in immediate spatial proximity to each other (independent of whether surface or bulk reactions are considered), the reactants' mobilities strongly affect the formation ratios of particular molecular species. Such information is extremely difficult to obtain from experiments which makes direct simulation an attractive and often the only alternative. Some of the models explicitly assume a certain mobility of the participating reagents which is not guaranteed and incompletely understood at low temperatures characteristic for such environments. One such relationship for the hopping probability $P$ is $P = \exp\left(-[E_D/200] \cdot \Delta x\right)$ which depends on the desorption energy

 

($E_D$) of the species of interest relative to water, and the average distance $\Delta x$ between adsorption sites.[7] However, since in amorphous ice - which is the form of radiatively processed water ices - $\Delta x$ is rather characterized by a *distribution* and $E_D$ are often incompletely known from direct measurements for the species of interest, a considerable amount of uncertainty is involved in employing $P$ from such estimates. Hence, more direct approaches for estimating the mobility of relevant chemical reagents is desirable. One such method are atomistic molecular dynamics simulations. However, it is worthwhile to mention that very recently an experimental characterization of oxygen atom surface diffusion on amorphous water ices has been carried out which reports an activation energy between 0.5 and 1 kcal/mol for surface diffusion.[20]

Depending on the particular reaction network model used, free atomic oxygen is implicated in several elementary steps in water formation under interstellar conditions. One possibility is the sequential addition of hydrogen atoms to adsorbed oxygen atoms $O_{ads}$ [14,17,21]

$$O_{ads} + H_{ads} \rightarrow OH_{ads} \quad (1)$$

$$OH_{ads} + H_{ads} \rightarrow H_2O_{ads} \quad (2)$$

This is possible as the number density of atomic oxygen is among the largest of all elements (several $10^{-4}$ relative to $n_H$) in the interstellar space.[22,23] Also, depending on the astrophysical environment, $n$(O) can exceed $n$(H) and be comparable to $n$(CO).[23] The adsorbed oxygen atom on the amorphous ice may diffuse into the bulk ice and then migrate inside it. In one scenario (the "$O_2$ route") atomic oxygen is involved in the formation of $O_2$ and $O_3$ from their relative atomic and molecular precursors.[7,17,24] Under these circumstances, oxygen diffusion is relevant. On the other hand, if hydrogen atoms diffuse on the surface (or within bulk) and react with a localized oxygen atom ("oxygen route")[14] the mobility of the oxygen atoms is probably less relevant although it may still contribute to enhancing formation ratios of OH which is the first step for $H_2O$ production.

Other reactions that have been proposed to be involved in water formation, in which atomic oxygen does not directly participate, include the collision of $H_2$ and OH to form H+$H_2O$, and $H_2O_2$ + H $\rightarrow$ $H_2O$ + OH.[7] Finally, water could also be formed by addition of

hydrogen atoms to molecular oxygen[19,25]

$$H + O_{2,s} \rightarrow HO_{2,ads} \quad (3)$$

$$H + HO_{2,ads} \rightarrow H_2O_{2,ads} \quad (4)$$

$$H + H_2O_{2,ads} \rightarrow H_2O_{ads} + OH_{ads} \quad (5)$$

where $O_2$ is formed from the collision of two atomic oxygens. Hence, oxygen mobility is relevant at various levels in water synthesis under interstellar conditions.

As it is difficult to investigate the reactions or movement of the atomic species occurring remotely, laboratory experiments and computer simulations are essential to elucidate elementary processes and understand the process in more detail. In the present work, classical molecular dynamics (MD) simulations are used to estimate the mobility of atomic oxygen in bulk amorphous water ice at low temperature. As evidenced above, the migration of atomic oxygen is essential for water formation for several scenarios but quantitative numbers whether and to what extent it is mobile are lacking. In addition, the free energy barrier for the migration and the solvation free energy of the atomic oxygen in amorphous ice is estimated.

One essential ingredient in atomistic simulations is the quantitative and meaningful description of the intermolecular interactions. In conventional MD simulations, point charges are used to describe the electrostatic interactions in the system. A conventional point charge model is not suitable to describe atomic oxygen, as its total charge is zero. However, an oxygen atom in its ground electronic state ($^3$P) has two unpaired electrons and the electronic density is not spherically symmetric, which gives rise to a nonzero quadrupole moment on the atom. Such nonspherical charge distributions can be conveniently described within an atomic orbital framework which is, for example, provided by a multipolar representation. As has been shown in previous works,[26–29] the inclusion of multipole moments on the simulation systems can give more realistic results in the MD simulations. It has been shown recently that a multipolar force field with physically motivated parametrization can describe nuclear dynamics, spectroscopy, and thermodynamics quantitatively.[28,30,31]

In the present work a quadrupolar model for atomic oxygen is employed to realistically describe the dynamics and cavity migration in

 

amorphous ice at low temperatures. First, the computational methods are presented. Next, oxygen migration and its solvation free energy are characterized and finally conclusions are drawn.

## 2 Computational Methods

### 2.1 Intermolecular Interactions and Molecular Dynamics

All molecular dynamics (MD) simulations have been carried out with the CHARMM program[32] with provisions for multipolar interactions.[26] The system considered includes one oxygen atom, O, inside a cubic box of amorphous ice of edge length $\approx 31$ Å containing 997 water molecules. The density of the system is that of water at standard conditions. A snapshot of the simulation system is shown in Figure 1.

All simulations were carried out with periodic boundary conditions (PBCs). Nonbonded interactions (electrostatic and van der Waals) for particles whose interatomic distances are larger than 12 Å were ignored. A shift function was used for the electrostatic interactions and the van der Waals interactions were switched between 10 and 12 Å. A Nosé-Hoover thermostat[33,34] was used in the $NVT$ simulations and the equations of motion were propagated with a time step of $\Delta t = 0.4$ fs to account for the flexible water molecules (see below).

For the water molecules, a flexible model based on the parametrization by Kumagai, Kawamura, and Yokokawa (KKY) was used.[35] The functional form of the KKY potential for the stretching and bending energies is

$$E_{\mathrm{str}} = D_e\{1 - \exp[-\beta(r - r_0)]\}^2 - D_e \tag{6}$$

and

$$E_{\mathrm{bend}} = 2f_k\sqrt{k_1 k_2}\,\sin^2(\theta - \theta_0) \tag{7}$$

where $k_i = 1/\{\exp[g_r(r_i - r_m)] + 1\}$, in which $r_i$ is the distance of one O–H bond of the water molecule and $g_r$ and $r_m$ are the force field parameters reported in the work of Kumagai et al.[35] The parameters used in the present work are identical except for the bending parameter ($f_k$) which needed to be changed to match the experimental bending frequency. As pointed out previously,[36] the value of $f_k$ from the original KKY parametrization seems to be several

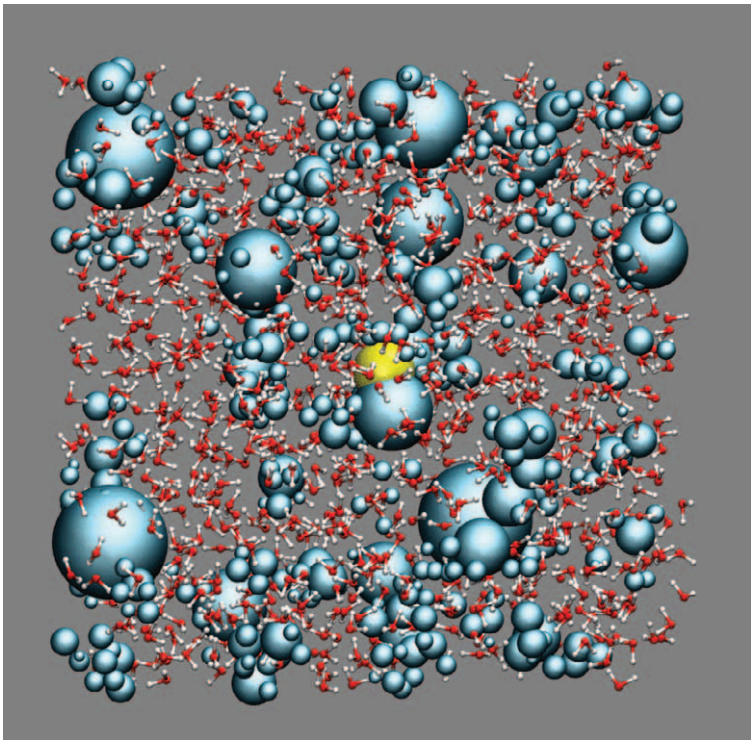

**Fig. 1** Lee and Meuwly
A snapshot of the system studied. The yellow sphere represents atomic oxygen and the cyan beads delineate the cavities in amorphous ice. Water molecules are shown in ball-and-stick representation.

orders of magnitude too large and overestimates the bending frequency. This is probably related to the fact that the original parameters were fitted to thermodynamic rather than spectroscopic data.[35,37] The present parametrization has also been used in recent work of water mobility at the solid/water interface and found to perform well for such applications.[?]

Electrostatic interactions for water were described by geometry-independent multipole moments previously determined.[27] Point dipole and quadrupole moments were placed on the water oxygen atoms, in addition to the point charges. For water hydrogen atoms, only point charges were used. For the atomic oxygen, a point quadrupole moment was placed in order to describe its interactions with the water molecules more accurately, see below. Such a water model has been validated in spectroscopic simulations and correctly re-

 

produces experimentally known infrared spectra and water diffusion.[38,39]

For the MTP model of the oxygen atom, DFT/B3LYP calculations with the aug-cc-pVQZ basis set were carried out for a single oxygen atom using Gaussian 03 (G03).[40] The level of theory was chosen such as to be consistent with the electrostatics used for the water molecules. Then, the GDMA program[41] was used to obtain multipole parameters up to quadrupole moments. Only one component of the quadrupole tensor, $Q_{20} = -0.948\ ea_0^2$, is nonzero. As a comparison, values obtained from previous calculations are $-0.968$ (ROHF), $-1.021$ (CASSCF), and $-1.036$ (CASPT2) in atomic units.[42] As the quadrupole moment is the only nonvanishing contribution (except for van der Waals interactions) it is of interest to put this into context with other small molecules: the quadrupole moment for atomic oxygen is also comparable to that of molecular NO ($1.14\ ea_0^2$) and somewhat smaller that that of $CN^-$ ($3.67\ ea_0^2$).

When higher multipole moments are employed on interaction centers in MD simulations, local coordinate systems are required. They relate the orientation of the atom-centered MTPs (i.e. "orbitals") to the frame of the entire molecule and the laboratory frame.[43] As for a single atomic site no neighboring atoms rigidly linked to it exist, the instantaneous reference axis system needs to be set up differently.[29] In the present case, the direction of the axis which gives the lowest energy is determined by scanning the grid points of the solid angle given by HEALPix.[44] In the present work, grid points with $N_{\mathrm{side}} = 2$ were employed, which gives 48 pixels. Thanks to the symmetry of the oxygen atom and the grid points, only half of the pixels are required.

For the Lennard-Jones (LJ) parameters $\varepsilon$ and $r_{\mathrm{min}}$ of water, those of the TIP3P model were used in all simulations. For atomic oxygen the values from the universal force field (UFF)[45] were adopted, i.e. $\varepsilon = 0.060$ kcal/mol and $r_{\mathrm{min}}/2 = 1.75$ Å. Overall, the oxygen atoms interacts with its environment through charge-quadrupole and van der Waals ($O\text{-}O_{\mathrm{water}}$ and $O\text{-}H_{\mathrm{water}}$) interactions.

Atomistic simulations for a single oxygen atom in amorphous ice were started by an initial heating and equilibration simulation at 300 K. Then, the temperature of the system was quenched to 50, 100,

or 200 K. Upon cooling, the system was equilibrated for $\approx$ 20 ps of *NPT* simulations. Next, 4 ps of *NVT* equilibration were carried out, after which production simulations 100 ps in length followed. Overall, 80 independent trajectories, each 100 ps in length were run, totaling 8 ns of data from which the observables were determined. The arrangement and mobility of the water molecules can be seen in Figure 3. As ASW has no evident long range structure it is difficult to directly compare structural determinants. The distribution of pore sizes in the present work is reported in Figure 4 together with the typical separation between the pores. However, to the best of our knowledge no such information is available from direct experimentation. Nevertheless, it is worthwhile to mention that an early electron diffraction study at temperatures between 15 K and 188 K have found transitions between three amorphous forms of water ice $I_a$h (high-density amorphous ice), $I_a$l (low-density amorphous ice), and $I_a$r (restrained amorphous ice). It was suggested that the persistence of $I_a$r above 144 K explained anomalous gas retention and release from water-rich ices at temperatures above 150 K.[2]

For comparison, simulations with a conventional TIP3P water model were also carried out without any electrostatic interactions on the atomic oxygen, i.e. a standard force field model. Hence, the oxygen atom only interacted with its environment through van der Waals interactions between the water-oxygen and hydrogen atoms. For this, SHAKE[46,47] was used to constrain the bonds involving hydrogen atoms and the time step was increased to $\Delta t = 1$ fs.

## 2.2 Analysis and Determination of Observables

*Diffusion Coefficient:* Traditionally, the diffusion coefficient is determined from the mean square displacement.[48] As in the present case - diffusion of a particle in a constraining and slowly moving environment at low temperature - the process in question is activated (hopping of atomic oxygen from one cavity to another) and slow, such an analysis would require extremely long MD simulations. Hence, a different approach was pursued here as described in more detail below. Furthermore, simulations with varying interaction strengths between the oxygen atom and the water matrix are also carried out whereby the nonbonded interactions were scaled by factors including 0.2, 0.4, 0.6, and 0.8, respectively. This will also

 

facilitate diffusion of the oxygen atom and improve statistics which can be extrapolated to the full interaction strength.

The number of jumps of the atomic oxygen from one cavity to another in the amorphous ice was determined from the coordinates of the atomic oxygen. First, a running average over 4000 steps was calculated for each coordinate of the atomic oxygen along the *x*-, *y*-, and *z*-directions, and averaged coordinates were taken every 200 steps. The unit vector in the direction of the displacement of the atomic oxygen was constructed for each pair of consecutive coordinate sets. Then the angle $\gamma$ between two consecutive unit vectors was calculated. If $\gamma \lesssim 78^\circ$, the atomic oxygen was regarded to be moving in the same direction. The value $78^\circ$ was determined from an analysis of the jump distances and directions and upon visual inspection of selected trajectories. If the oxygen atom moves in the same direction for more than 2000 steps (0.8 ps), this sequence of movements has been considered as a jump, as long as the total displacement is larger than 1.5 Å, which will be denoted as $\Delta r_{\mathrm{thr}}$. The average displacement over all the jumps has also been computed and used as the jump distance $\Lambda$.

Alternatively, a phenomenological model based on a jump frequency $\Gamma$ has been devised from which a diffusion coefficient $D$ has been estimated according to[37]

$$D = \alpha \Lambda^2 \Gamma, \tag{8}$$

where $\alpha$ is the number of equivalent paths for a jump and $\Lambda$ is the jump distance. For 2-dimensional diffusion in ice $\mathrm{I}_h$ $\alpha = 2$ has been employed[37] which is also the value used here. However, this value is probably larger in the present situation and could be optimized for the case of 3-dimensional diffusion in amorphous ice. As this is only a phenomenological analysis, and more rigorous treatments based on free energy simulations are discussed further below, no attempt was made to refine the value of $\alpha$. The diffusion coefficients obtained from this analysis are therefore lower bounds. The jump distance $\Lambda$ is obtained by averaging actual jump distances from the trajectories. The temperature dependence of $D(T)$ is assumed to follow an Arrhenius-type behaviour[37]

$$D = D_0 \exp\left(-\frac{E_a}{RT}\right), \tag{9}$$

where $D_0$ is a constant, $E_a$ the activation energy, and $R$ the gas constant. From this expression, an activation energy can be estimated based on the number of jumps observed in the simulations.

*Free Energy Simulations:* A more rigorous estimate for the transition barrier heights is available from free energy simulations. Such techniques can also be employed to determine solvation free energies and are briefly summarized below.

Umbrella sampling (US) is used to estimate the free energy barrier for the movement of an oxygen atom from one cavity to another. US employs an external biasing potential $U^{(i)}(\delta) = K^{(i)}(\delta - \delta_0^{(i)})^2$ to constrain a system around a value $\delta_0^{(i)}$ of the reaction coordinate and then determines the probability distribution $P(\delta_A)$ to find the system at reaction coordinate $\delta = \delta_A$ (state A). For each window $i$ a corresponding free energy

$$F^{(i)}(\delta) = -k_B T \ln[P^{(i)}(\delta)] - U^{(i)}(\delta) + C^{(i)} \qquad (10)$$

can be obtained, where $C^{(i)}$ is a constant for the $i$-th window and $P^{(i)}(\delta)$ is the equilibrium distribution in the presence of the biasing potential $U^{(i)}(\delta)$ for the same window. The constant $C^{(i)}$ is in general different for each window and can be determined using Weighted Histogram Analysis Method (WHAM).[49,50] In the present work, $\delta$ is the distance between the atomic oxygen and the plane at the barrier separating the two cavities which can hold the oxygen atom. The plane is composed of 3 water oxygen atoms and is approximately perpendicular to the path followed by the oxygen atom when it makes a transition from one cavity to another. Overall, 17 windows with $\delta_0$ values ranging from $-4.0$ to 4.0 Å with a separation of 0.5 Å and a force constant of $K = 3.0$ kcal/mol·Å$^2$ for all intervals were employed. For each window, the system was equilibrated for 2 ps with the umbrella potential, which was followed by 40-ps of simulation during which data collection took place. Six independent snapshots from different jump instances at 100 K with full intermolecular interactions were selected for the umbrella sampling simulations.

Free energy differences between two states A and B can also be determined from alternative methods, including Thermodynamic integration (TI)[51,52], free energy perturbation (FEP) simulations,[53] or the Bennett acceptance ratio (BAR) approach.[54] Several meth-

 

ods are used in order to verify consistency between the results obtained. In TI a coupling parameter $\lambda$ is introduced, which is 0 for A (reactant - or oxygen in one cavity) and 1 for B (product - or oxygen in another (neighboring) cavity) and the potential energy of the system is written as $U(\mathbf{r}_1,\ldots,\mathbf{r}_N,\lambda) = (1-\lambda)U_{\rm A}(\mathbf{r}_1,\ldots,\mathbf{r}_N) + \lambda U_{\rm B}(\mathbf{r}_1,\ldots,\mathbf{r}_N)$. Then, the free energy change for the reaction A $\rightarrow$ B is obtained from

$$\Delta F({\rm A}\rightarrow{\rm B}) = \int_0^1 d\lambda \left\langle \frac{\partial U}{\partial \lambda} \right\rangle_\lambda = \int_0^1 d\lambda \, \langle U_{\rm B} - U_{\rm A}\rangle_\lambda = \int_0^1 d\lambda \, \langle U_{\rm ow}\rangle_\lambda , \tag{11}$$

where $U$ is a potential energy, $\langle\cdots\rangle_\lambda$ denotes an ensemble average at $\lambda$, and $U_{\rm ow}$ are the solute-solvent interactions.[31] The thermodynamic integral is decomposed into contributions $\langle U_{\rm ow}\rangle_\lambda$ for different $\lambda-$values between 0 and 1 where $\langle\cdots\rangle_\lambda$ is computed by averaging over the distribution $\exp[-\beta U(\mathbf{r}_1,\ldots,\mathbf{r}_N,\lambda)]$ from the simulations performed at a particular value of $\lambda$ which include (0.2, 0.4, 0.6, 0.8, and 1.0) in the present work.

In FEP the free energy difference between states A and B can be computed from

$$\Delta F({\rm A}\rightarrow{\rm B}) = -k_{\rm B}T \ln \left\langle e^{-\beta(U_{\rm B}-U_{\rm A})} \right\rangle_{\rm A} . \tag{12}$$

While the equation above can be applied if states A and B are very similar, they can be quite different in many cases, such as the system considered in the current work. To reduce the error, the path from A to B is divided into multiple steps, and the free energy difference for the change from A to B is obtained by summing the free energy differences between all consecutive steps. The same $\lambda$ values as used in the thermodynamic integration are used for FEP in the present work, so as to reuse the trajectories generated for the thermodynamic integration.

The BAR method is an algorithm which uses the fact that any function $f(x)$ satisfying $f(x)/f(-x) = e^{-x}$ and for any value of $C$

$$e^{-\beta(\Delta F - C)} = \frac{\langle f(\beta(U_{\rm B}-U_{\rm A}-C))\rangle_{\rm A}}{\langle f(\beta(U_{\rm A}-U_{\rm B}+C))\rangle_{\rm B}}, \tag{13}$$

holds. Here, $\Delta F$ is the free energy difference and $U_{\rm A}$ is the potential energy of system A. The optimal choice of $f(x)$ and $C$ has been shown to be $f(x) = 1/(1+e^x)$ and $C \approx \Delta F$.[54] Similarly to the

case of FEP, the path from A to B is divided into multiple steps, and Eq. (13) is applied to each consecutive steps. The free energy change from A to B is obtained by summing free energy differences between all consecutive steps. The same trajectories are used for TI, FEP, and BAR methods.

## 3 Results and Discussion

### 3.1 Oxygen migration

The movement of atomic oxygen in bulk amorphous water ice at temperatures of 50, 100, and 200 K was investigated from multiple independent MD simulations each 100 ps in length. The temperature range chosen covers the high side of astrophysically relevant temperatures, which is typically $T \approx 10$ K[17] up to $T \lesssim 50$ K[11] and goes up to temperatures for which ASW are assumed and have been reported to exist.[2] Such relatively high temperatures in the simulations are also called for as the expected mobility of the oxygen atoms is expected to be slow and very long simulation times would be required to observe transitions between cavities in unbiased simulations at all. From the temperature dependence of the computed observables one may then also extrapolate the behaviour at lower temperatures.

Figure 2 shows the temporal variation of the $x-$, $y-$, and $z-$coordinates of the atomic oxygen at 100 K from a representative 100-ps simulation with the KKY water model. Typical jumps, which occur long all three spatial directions in the present case, range over 2 to 4 Å, see Figure 2 The traces also establish that the migration is an activated, jump-like process and does not resemble conventional diffusion.

2-dimensional projections of an oxygen translocation at the three simulation temperatures are reported in Figure 3. On the time scale of the simulation (100 ps) at 100 K (middle panel) the positions of the water molecules are quasi-stationary as is expected for ice, whereby the oxygen atom visits at least three different sites within the ice matrix. Also, the irregular distribution of the water molecules in both, the $xy-$ and $xz-$planes is evident. At the temperatures of interest, spontaneous migration of atomic oxygen in amorphous ice

 

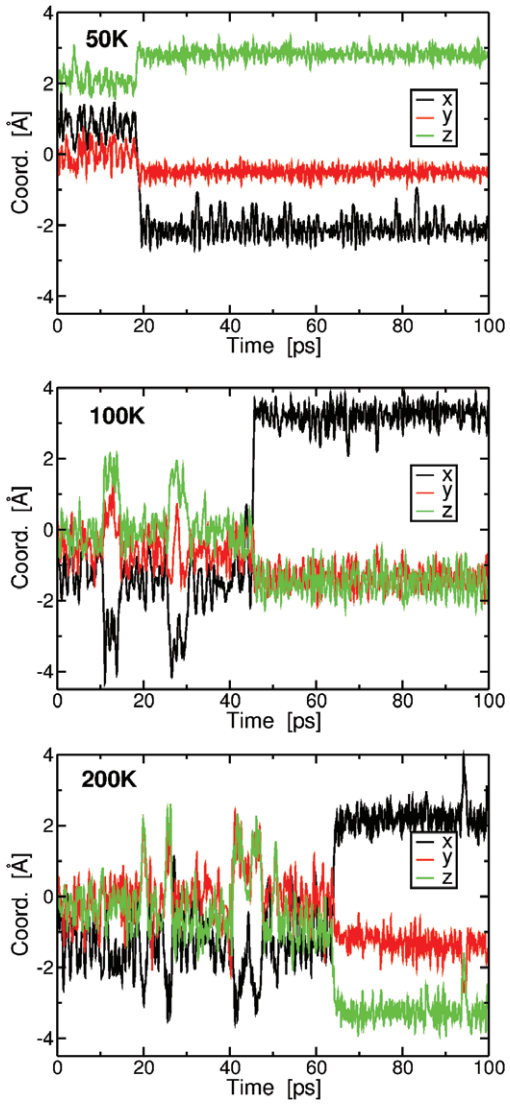


**Fig. 2** Lee and Meuwly
Temporal variation of the $x-$, $y-$, and $z-$coordinates of atomic oxygen along a 100-ps simulation at 100 K with full intermolecular interactions using KKY water model.

between neighboring cavities was observed between 10 – 30 times on the 2 ns timescale. To increase the number of transitions, simulations were also carried out by decreasing the interaction strength between the atomic oxygen and water molecules, as the barrier height for the transition is directly influenced by the $O\cdots H_2O$ interactions. This was achieved by simultaneously scaling the electrostatic and van der Waals interactions by a constant factor $\lambda < 1$. Specifically, simulations of 2 ns ($20 \times 100$ps) each were carried out with $\lambda = 0.2$, 0.4, 0.6 and 0.8.

The migration of oxygen atoms in amorphous ice directly depends on the size and distribution of the cavities. For this, the cavities were analyzed in more detail. The position and volumes of the cavities were determined with the SURFNET program,[55] which can detect the cavities in a heterogeneous distribution of matter, such as in amorphous ice or in proteins by placing probe spheres at specific locations which are subsequently grown until they fill space. The volumes of cavities inside amorphous ice was computed for cavities whose volumes are larger than 20 $Å^3$, from the snapshots at 50, 100, and 200 K, respectively. Only snapshots obtained with full nonbonded interactions between atomic oxygen and water were considered. The distribution of the cavity volumina is shown in the inset of Figure 4. A useful measure for the probability to find a cavity within a distance $r$ of another cavity is provided by the radial distribution function $g(r)$ of the cavity centers. From the same trajectories used for the cavity volume analysis, their radial distribution function was determined, and it is shown in Figure 4.

### 3.2 Oxygen Diffusion

The number of transitions for atomic oxygen from $80 \times 100$ ps simulations in amorphous ice is shown in Figure 5 at various temperatures. As expected, the number of transitions is larger at higher temperature and at decreased intermolecular interaction strength. At 50 K, the number of transitions is generally small, $\approx 5$ transitions per nanosecond) and increases with increasing temperature. Still, due to the small number of transitions, the error in the number of jumps/ns is appreciable. As MTP simulations are quite time consuming, additional $80 \times 250$ ps (i.e. 20 ns in total) simulations without MTP on atomic oxygen and using the TIP3P water model

 

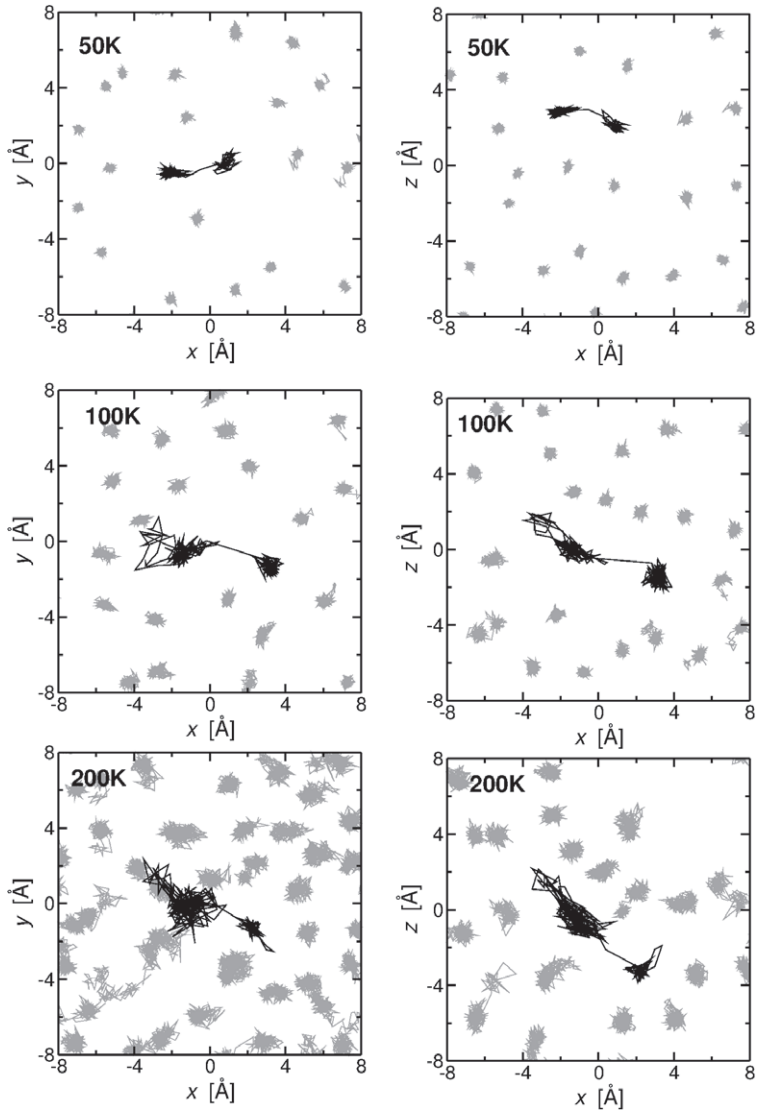


**Fig. 3** Lee and Meuwly
Trajectory of atomic oxygen projected on the $xy-$ and $xz-$planes shown in black in the left and right panels, respectively, from a 100-ps simulation. The trajectories of water oxygen atoms located in the range -2.0 Å$< z <$ 0.5 Å or -2.0 Å$< y <$ 0.5 Å are shown as gray lines.

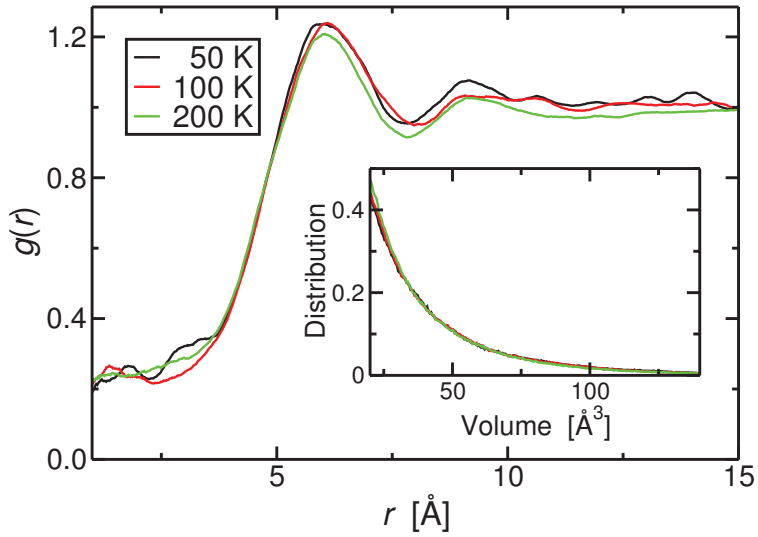


**Fig. 4** Lee and Meuwly
Radial distribution functions of cavities in amorphous ice at 50, 100, and 200 K are shown. The inset shows the distribution of volumes of cavities in amorphous ice at 50, 100, and 200 K.

with SHAKE were also carried out. These simulations provide an independent validation and assessment of the importance of refined electrostatics on the oxygen atom. The result is also reported in Figure 5. Due to the increased length of the simulations and the improved statistics, the results are smoother. However, overall the results from MTP and point charge simulations are similar and suggest that 10 ns simulations are capable of qualitatively capturing oxygen migration in amorphous ice.

To estimate the error bar of the number of jumps obtained from the simulations, the entire data set was divided into 4 subgroups, and the number of jumps per nanosecond was determined for each subgroup. From this, the standard deviation was determined. The approximate error bar thus obtained for the $80 \times 100$ ps simulations with (MTP and KKY for water) is $\approx 13$ ns$^{-1}$, whereas for the $80 \times 250$ ps simulations (standard electrostatics and TIP3P) the error is 4 ns$^{-1}$. The error bars tend to decrease at higher temperature. The positions of water molecules in the amorphous ice for different $\lambda$ values are similar as the simulations start from the same initial structures. While separate equilibrations for each $\lambda$ value were carried out, water molecules do not move away under the conditions

 

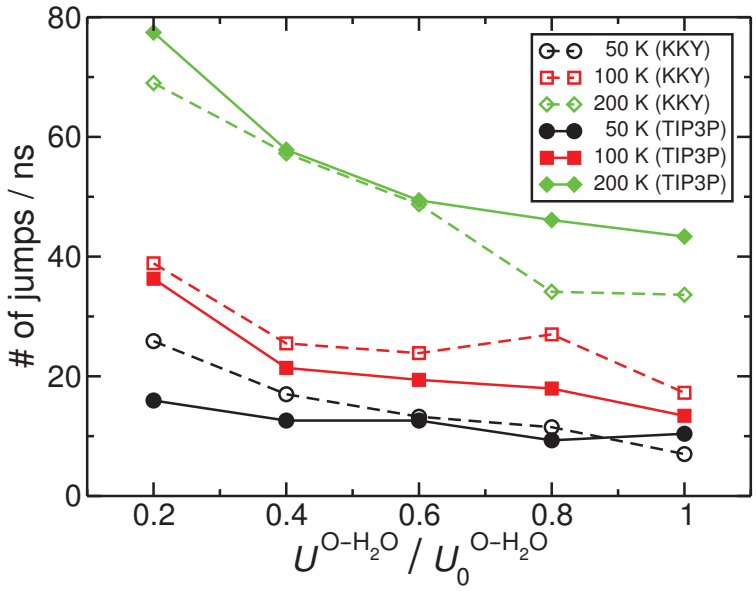


**Fig. 5** Lee and Meuwly
Average number of jumps per nanosecond of atomic oxygen between cavities in the amorphous ice during the 80 × 100 ps simulations (MTP with KKY, dashed lines) and 80 × 250 ps simulations (standard electrostatics with TIP3P water model, solid lines) at 50, 100, and 200 K, shown in black, red, and green, respectively. The interaction potential between the atomic oxygen and the water molecules, $U^{O\cdots H_2O}$, was scaled by 0.2, 0.4, 0.6, 0.8, and 1.0 times the original value, $U_0^{O\cdots H_2O}$.

used for the simulations.

To quantify the free energy change along the transition paths of atomic oxygen from one cavity to another, umbrella sampling as described in the Methods section was used. A typical computed free energy profile is shown in Figure 6. Umbrella sampling was carried out for both, the MTP oxygen with the KKY water model and PC oxygen with the TIP3P water model. For direct comparison, the same initial coordinate set was used for both simulations. the barriers range from 0.5 to 1.5 kcal/mol. It is noted that the barrier height is lower in the case of a conventional force field for the oxygen atom together with the TIP3P water model, which does not involve multipolar interactions. This is also what has been found in simulations of CO in Myoglobin.[56] The minima along the migration pathway occur at similar reaction coordinates but the the MTP charge model stabilization in the local minima is more pronounced.

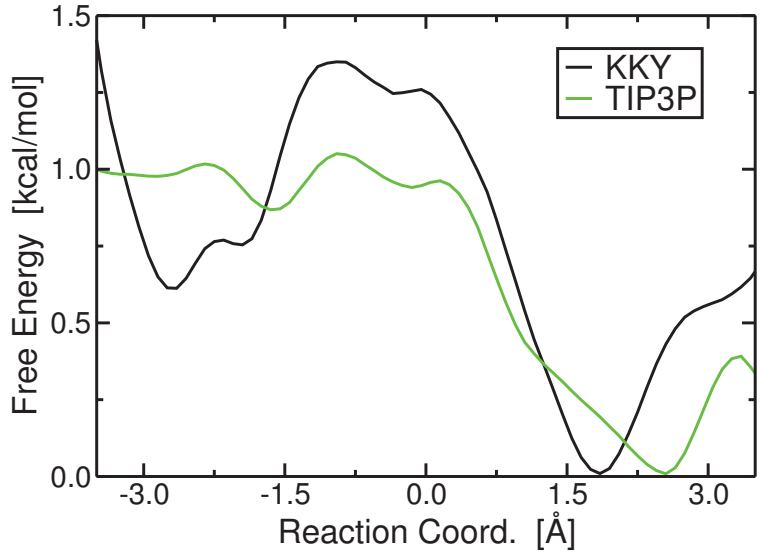


**Fig. 6** Lee and Meuwly
Free energy profile for a single oxygen migration step from one cavity to the nearest neighbor at 100 K. Umbrella sampling was used for 40 ps for each window with full van der Waals and electrostatic interactions with KKY water model (black curve). For comparison, the same calculations were carried out with a PC model for oxygen and the TIP3P water model starting from the same initial coordinate file (green curve). The profiles were obtained using 17 windows along the progression coordinate.



 

For the particular situation encountered here, a local maximum in the free energy profile is found around $\delta \approx -0.9$ Å. To either side of this maximum, local minima of different depths are found. For the umbrella sampling shown in Figure 6, the estimated barrier height from the right is $\approx 1.4$ kcal/mol, while that from the left is $\approx 0.8$ kcal/mol. The values of barrier heights from six different sets of umbrella sampling simulations range from 0.7 to 1.9 kcal/mol (0.7, 0.9, 1.3, 1.4, 1.8 and 1.9 kcal/mol), hence the situation in Figure 6 is a typical one.

The diffusion coefficients at different temperatures have also been estimated using the phenomenological relationship from Eq. (8) with $\alpha = 2$ and the values of $\Lambda$ and $\Gamma$ obtained from the simulations with full intermolecular interactions ($\Lambda \approx 2.1$, 2.2, and 2.7 Å and $\Gamma \approx 7.0$, 17.2, and 33.6 $ns^{-1}$ at 50, 100, and 200 K, respectively). This yields $D = 60$, 174, and 480 $Å^2$/ns at 50, 100, and 200 K, respectively. From the diffusion coefficients $D(T)$ at different temperatures, see Figure 7, an activation energy $E_a \approx 0.27$ kcal/mol is found.

To better understand the effect of selecting different jumps on the activation energy, additional analyses with $\Delta r_{thr} = 2.0$ Å was carried out. This corresponds to excluding smaller jumps included in the previous analysis with $\Delta r_{thr} = 1.5$ Å. The activation energy with $\Delta r_{thr} = 2.0$ Å is 0.31 kcal/mol, while that with $\Delta r_{thr} = 1.5$ Å is 0.27 kcal/mol, as displayed in Figure 7. This shows that selecting only the pronounced jumps increases the activation energy. It is also noted that the activation energy obtained from trajectories generated with the KKY water model is higher than that with the TIP3P model, which is in agreement with the change in barrier height computed from umbrella sampling simulations using KKY and TIP3P models.

When comparing the barrier height from the umbrella sampling with the activation energy $E_a \approx 0.27$ kcal/mol from an Arrhenius-like expression, it is found that the magnitude of the barrier height is larger than the activation energy. The difference may be caused by the applied umbrella potential which can affect the local structure in the umbrella sampling simulations and thus can lead to changes in the barrier height. However, as no appreciable water restructuring was observed during the umbrella sampling simulations, this is

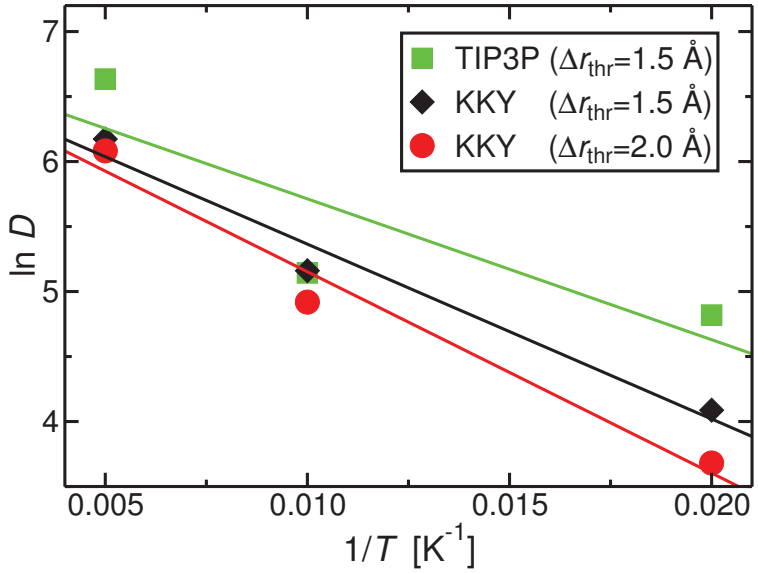


**Fig. 7** Lee and Meuwly
The plot of $\ln D$ vs. $1/T$ is computed from trajectories generated with TIP3P water model (green) and those with KKY water model (black and red). The green and black lines were computed with $\Delta r_{thr} = 1.5$ Å (see "Computational Methods" section) and the red line with $\Delta r_{thr} = 2.0$ Å. The estimated $E_a$ values from the slopes calculated from the linear regressions are 0.22, 0.27, and 0.31 (green, black, and red, respectively).



 

less likely. Rather, the phenomenological character of Eq. (8), insufficient sampling of the unbiased MD simulations and incomplete knowledge about the number of independent paths ($\alpha$) suggest that typical barrier heights for oxygen migration in amorphous ice are of the order of 1 kcal/mol which agrees quite favourably with recent experiments for oxygen diffusion on water ice at temperatures between 6 and 25 K which found a best-fit value for the activation energy of 520 K (1.0 kcal/mol) and a range of acceptable model parameters between 300 and 500 K (0.6 to 1.0 kcal/mol).[20] Previous values employed in astrophysical models and reported in the literature range from 240 K (0.5 kcal/mol) (oxygen diffusion *in* solid Xenon)[57] to 400 K (0.8 kcal/mol)[17] and 900 K (1.8 kcal/mol).[58]

As the linearity in $\ln D$ vs. $1/T$ shown in Figure 7 is not fully apparent, errors in the estimated activation energy from the slope cannot be avoided. On the other hand, for the umbrella sampling, more pronounced jumps were selected which are expected to exhibit larger barrier heights. Therefore, the barrier height computed from umbrella sampling is expected to be somewhat larger than the activation energy estimated from the temperature dependence of the diffusion coefficient.

### 3.3 Solvation free energy

The solvation free energy of atomic oxygen in amorphous ice was computed using TI, FEP, and BAR methods. The results are summarized in Table 1. The computed solvation free energy of atomic oxygen is considerably smaller than that of diatomic anions in water,[31] due to the absence of charge. The differences among the results obtained from different methods are larger in the range of $\lambda$ between 0.0 and 0.2, while the results from various methods coincide within less than 0.06 kcal/mol for each interval in the case of intervals with $\lambda \geq 0.2$, as can be seen in the table. Similar behavior has also been observed in previous work on the solvation free energy of cyanide or hydroxide ion in water,[31] where a much finer grid of $\lambda-$values was used for $\lambda \leq 0.1$ in order to increase the accuracy in this range. No finer grids were employed in the present calculations as the magnitude of the free energy is small, which makes it difficult to decrease the relative error due to the inherent inaccuracy in the free energy calculation. In the case of TI, it is also possible to decompose the contribution to the solvation free energy into the electrostatic interactions (elec) and van der Waals

interactions (vdW). The decomposed values in kcal/mol are -0.88 (elec) and -0.85 (vdW) at 50 K, -0.84 (elec) and -0.60 (vdW) at 100 K, and -0.89 (elec) and -0.07 (vdW) at 200 K. Without quadrupole moment on the oxygen atom, the contribution of the electrostatic interactions is zero. It is clear that electrostatic interactions play a significant role, further stabilizing the atom in the environment of the amorphous ice and this is what should be observed from comparing simulation results with and without MTP electrostatics as is done further below.

**Table 1** Solvation free energies of atomic oxygen in amorphous ice computed with TI, FEP, and BAR at 50, 100, and 200 K are given in kcal/mol. The values from each λ interval and the sum over all intervals are shown.

| Temp. | Range of λ | TI | FEP | BAR |
|---|---|---|---|---|
| 50 K | 0.0 – 0.2 | -0.23 | 0.03 | 0.03 |
| | 0.2 – 0.4 | -0.29 | -0.29 | -0.29 |
| | 0.4 – 0.6 | -0.34 | -0.38 | -0.34 |
| | 0.6 – 0.8 | -0.40 | -0.42 | -0.39 |
| | 0.8 – 1.0 | -0.46 | -0.48 | -0.44 |
| | Total | -1.72 | -1.54 | -1.43 |
| 100 K | 0.0 – 0.2 | -0.15 | 0.80 | 0.80 |
| | 0.2 – 0.4 | -0.22 | -0.23 | -0.24 |
| | 0.4 – 0.6 | -0.29 | -0.32 | -0.31 |
| | 0.6 – 0.8 | -0.36 | -0.36 | -0.35 |
| | 0.8 – 1.0 | -0.43 | -0.42 | -0.41 |
| | Total | -1.43 | -0.53 | -0.51 |
| 200 K | 0.0 – 0.2 | -0.02 | 0.84 | 0.84 |
| | 0.2 – 0.4 | -0.10 | -0.12 | -0.12 |
| | 0.4 – 0.6 | -0.19 | -0.25 | -0.25 |
| | 0.6 – 0.8 | -0.28 | -0.31 | -0.31 |
| | 0.8 – 1.0 | -0.37 | -0.36 | -0.35 |
| | Total | -0.97 | -0.19 | -0.19 |

## 4 Conclusions

Classical MD simulations of atomic oxygen migration in amorphous ice using physically motivated force fields establish that intersite hopping occurs on the sub-nanosecond time scale at low temperatures ($T \leq 200$ K) with rates ranging from 4.5 to 15.5 $ns^{-1}$. The

 

barrier heights from the present work are $\approx$ 1 kcal/mol which compares with estimates of 0.5 kcal/mol to 1.8 kcal/mol from previous work and most favourably with a recent experimental study of oxygen on an amorphous water surface.[20] Together with the present findings (sub-kcal/mol activation energy and favourable solvation of oxygen in ASW) these insights suggest that oxygen-driven chemistry may play a more important role in interstellar environments than previously assumed.

The fact that conventional point charge force fields underestimate barrier heights by up to 50 % compared to MTP-based models is consistent with findings for carbon monoxide migration in myoglobin for which PC-based force fields also systematically underestimate migration barriers.[56] Free energy barriers computed from rigorous umbrella sampling simulations are larger than activation energies estimated from a phenomenological model based on the number of intersite jumps and fitting of the Arrhenius-like equation to the temperature-dependence of the diffusion coefficient. This difference may be attributed to insufficient statistics in counting the number of jumps for calculating the diffusion coefficient and the assumed number of pathways $\alpha$ between two neighboring sites.

The results of the present study are essential for rationalizing the formation and abundances of oxygen-containing molecular species in cold interstellar environments. It was generally assumed that the chemistry in such environments is primarily driven by hydrogen diffusion. However, given that the number densities of atomic hydrogen and atomic oxygen are comparable[23] and noting that the barrier for oxygen migration on[20] and in (this work) ASW is of the order of 1 kcal/mol or below, oxygen chemistry will play an important role in both, the formation of water (through the $O_2$ pathway) and the synthesis of larger organic molecules. It will be interesting to extend the present work to oxygen diffusion *on* ASW surfaces, which has already been done for CO diffusion.[59]

## Acknowledgments

The authors gratefully acknowledge financial support from the Swiss National Science Foundation through grant 200021-117810 and to the NCCR-MUST. The authors thank Dr. T. Nagy for discussions.

## References


1 W. Hagen, A. Tielens and J. Greenberg, *Chem. Phys.*, 1981, **56**, 367–379.
2 P. Jenniskens and D. Blake, *Science*, 1994, **265**, 753–756.
3 J. B. Bossa, K. Isokoski, M. S. de Valois and H. Linnartz, *Astron. Astrophys.*, 2012, **545**, A82.
4 A. Bar-Nun, J. Dror, E. Kochavi and D. Laufer, *Phys. Rev. B*, 1987, **35**, 2427–2435.
5 Y. Oba, N. Miyauchi, H. Hidaka, T. Chigai, N. Watanabe and A. Kouchi, *Astrophys. J.*, 2009, **701**, 464–470.
6 J. Keane, A. Tielens, A. Boogert, W. Schutte and D. Whittet, *Astron. Astrophys.*, 2001, **376**, 254–270.
7 H. M. Cuppen and E. Herbst, *Astrophys. J.*, 2007, **668**, 294–309.
8 A. G. G. M. Tielens, *Rev. Mod. Phys.*, 2013, **85**, 1021–1081.
9 N. Miyauchi, H. Hidaka, T. Chigai, A. Nagaoka, N. Watanabe and A. Kouchi, *Chem. Phys. Lett.*, 2008, **456**, 27–30.
10 R. Papoular, *Mon. Not. R. Astron. Soc.*, 2005, **362**, 489–497.
11 N. Flagey, P. F. Goldsmith, D. C. Lis, M. Gerin, D. Neufeld, P. Sonnentrucker, M. De Luca, B. Godard, J. R. Goicoechea, R. Monje and T. G. Phillips, *Astrophys. J.*, 2013, **762**, 11.
12 K. Hiraoka, T. Miyagoshi, T. Takayama, K. Yamamoto and Y. Kihara, *Astrophys. J.*, 1998, **498**, 710–715.
13 H. Mokrane, H. Chaabouni, M. Accolla, E. Congiu, F. Dulieu, M. Chehrouri and J. L. Lemaire, *Astrophys. J. Lett.*, 2009, **705**, L195–L198.
14 F. Dulieu, L. Amiaud, E. Congiu, J.-H. Fillion, E. Matar, A. Momeni, V. Pirronello and J. L. Lemaire, *Astron. Astrophys.*, 2010, **512**, A30.
15 C. Romanzin, S. Ioppolo, H. M. Cuppen, E. F. van Dishoeck and H. Linnartz, *J. Chem. Phys.*, 2011, **134**, 084504.
16 H. M. Cuppen, S. Ioppolo, C. Romanzin and H. Linnartz, *Phys. Chem. Chem. Phys.*, 2010, **12**, 12077–12088.
17 A. G. G. M. Tielens and W. Hagen, *Astron. Astrophys.*, 1982, **114**, 245–260.
18 H. M. Cuppen and E. Herbst, *Astrophys. J.*, 2007, **668**, 294–309.
19 S. Ioppolo, H. M. Cuppen, C. Romanzin, E. F. van Dishoeck and H. Linnartz, *Astrophys. J.*, 2008, **686**, 1474–1479.
20 M. Minissale, E. Congiu, S. Baouche, H. Chaabouni, A. Moudens, F. Dulieu, M. Accolla, S. Cazaux, G. Manico and V. Pirronello, *Phys. Rev. Lett.*, 2013, **111**, 053201.
21 T. P. M. Goumans, C. R. A. Catlow, W. A. Brown, J. Kästner and P. Sherwood, *Phys. Chem. Chem. Phys.*, 2009, **11**, 5431–5436.
22 V. Wakelam and E. Herbst, *Astrophys. J.*, 2008, **680**, 371–383.
23 P. Caselli, T. Stantcheva, O. Shalabiea, V. Shematovich and E. Herbst, *Planet. Space Sci.*, 2002, **50**, 1257–1266.
24 S. Ioppolo, H. M. Cuppen, C. Romanzin, E. F. van Dishoeck and H. Linnartz, *Phys. Chem. Chem. Phys.*, 2010, **12**, 12065–12076.
25 N. Miyauchi, H. Hidaka, T. Chigai, A. Nagaoka, N. Watanabe and A. Kouchi, *Chem. Phys. Lett.*, 2008, **456**, 27–30.
26 N. Plattner and M. Meuwly, *Biophys. J.*, 2008, **94**, 2505–2515.
27 N. Plattner, M. W. Lee and M. Meuwly, *Faraday Discuss.*, 2010, **147**, 217–230.
28 M. W. Lee and M. Meuwly, *J. Phys. Chem. A*, 2011, **115**, 5053–5061.
29 M. W. Lee, N. Plattner and M. Meuwly, *Phys. Chem. Chem. Phys.*, 2012, **14**, 15464–15474.
30 M. W. Lee, J. K. Carr, M. Göllner, P. Hamm and M. Meuwly, *J. Chem. Phys.*, 2013, **139**, 054506.
31 M. W. Lee and M. Meuwly, *Phys. Chem. Chem. Phys.*, 2013, **15**, 20303–20312.
32 B. R. Brooks, C. L. Brooks, III, A. D. Mackerell, Jr., L. Nilsson, R. J. Petrella, B. Roux, Y. Won, G. Archontis, C. Bartels, S. Boresch, A. Caflisch, L. Caves, Q. Cui, A. R. Dinner, M. Feig, S. Fischer, J. Gao, M. Hodoscek, W. Im, K. Kuczera, T. Lazaridis, J. Ma, V. Ovchinnikov, E. Paci, R. W. Pastor, C. B. Post, J. Z. Pu, M. Schaefer, B. Tidor, R. M. Venable, H. L. Woodcock, X. Wu, W. Yang, D. M. York and M. Karplus, *J. Comp. Chem.*, 2009, **30**, 1545–1614.
33 S. Nosé, *J. Chem. Phys.*, 1984, **81**, 511–519.


 

34 W. G. Hoover, *Phys. Rev. A*, 1985, **31**, 1695–1697.
35 N. Kumagai, K. Kawamura and T. Yokokawa, *Mol. Sim.*, 1994, **12**, 177–186.
36 C. J. Burnham, J. C. Li and M. Leslie, *J. Phys. Chem. B*, 1997, **101**, 6192–6195.
37 T. Ikeda-Fukazawa, S. Horikawa, T. Hondoh and K. Kawamura, *J. Chem. Phys.*, 2002, **117**, 3886–3896.
38 J. J. Szymczak, F. D. Hofmann and M. Meuwly, *Phys. Chem. Chem. Phys.*, 2013, **15**, 6268–6277.
39 P. K. Gupta and M. Meuwly, *Faraday Discuss.*, 2013, in print.
40 M. J. Frisch, G. W. Trucks, H. B. Schlegel, et al., *Gaussian 03, Revision B.01*, Pittsburgh, PA, 2003.
41 A. J. Stone, *J. Chem. Theo. Comp.*, 2005, **1**, 1128–1132.
42 M. Medveď, P. W. Fowler and J. M. Hutson, *Mol. Phys.*, 2000, **98**, 453–463.
43 C. Kramer, P. Gedeck and M. Meuwly, *J. Chem. Theo. Comp.*, 2013, **9**, 1499–1511.
44 K. M. Górski, E. Hivon, A. J. Banday, B. D. Wandelt, F. K. Hansen, M. Reinecke and M. Bartelmann, *Astrophys. J.*, 2005, **622**, 759–771.
45 A. K. Rappé, C. J. Casewit, K. S. Colwell, W. A. Goddard, III and W. M. Skiff, *J. Am. Chem. Soc.*, 1992, **114**, 10024–10035.
46 J.-P. Ryckaert, G. Ciccotti and H. J. C. Berendsen, *J. Comp. Phys.*, 1977, **23**, 327–341.
47 M. Yoneya, H. J. C. Berendsen and K. Hirasawa, *Mol. Sim.*, 1994, **13**, 395–405.
48 D. Frenkel and B. Smit, *Understanding Molecular Simulation: From Algorithms to Applications*, Academic Press, New York, 1996.
49 S. Kumar, J. M. Rosenberg, D. Bouzida, R. H. Swendsen and P. A. Kollman, *J. Comp. Chem.*, 1992, **13**, 1011–1021.
50 S. Kumar, J. M. Rosenberg, D. Bouzida, R. H. Swendsen and P. A. Kollman, *J. Comp. Chem.*, 1995, **16**, 1339–1350.
51 J. G. Kirkwood, *J. Chem. Phys.*, 1935, **3**, 300–313.
52 T. P. Straatsma and J. A. McCammon, *J. Chem. Phys.*, 1991, **95**, 1175–1188.
53 R. W. Zwanzig, *J. Chem. Phys.*, 1954, **22**, 1420–1426.
54 C. H. Bennett, *J. Comp. Phys.*, 1976, **22**, 245–268.
55 R. A. Laskowski, *J. Mol. Graphics*, 1995, **13**, 323–330.
56 N. Plattner and M. Meuwly, *Biophys. J.*, 2012, **102**, 333–341.
57 A. Benderskii and C. Wight, *J. Chem. Phys.*, 1996, **104**, 85–94.
58 S. Cazaux, V. Cobut, M. Marseille, M. Spaans and P. Caselli, *Astron. Astrophys.*, 2010, **522**, A74.
59 N. Plattner, J. D. Doll and M. Meuwly, *J. Chem. Phys.*, 2010, **133**, 044506.